

Covalently Bridging Gaps in Single-Walled Carbon Nanotubes with Conducting Molecules

Xuefeng Guo,^{1,5} Joshua P. Small,^{2,5} Jennifer E. Klare,^{1,5} Yiliang Wang,^{1,5} Meninder S. Purewal,^{4,5} Iris W. Tam,^{1,5} Byung Hee Hong,^{2,5} Robert Caldwell,^{4,5} Limin Huang,^{4,5} Stephen O'Brien,^{4,5} Jiaming Yan,^{1,5} Ronald Breslow,^{1,5} Shalom J. Wind,^{4,5} James Hone,^{3,5} Philip Kim,^{2,5*} Colin Nuckolls^{1,5*}

Molecular electronics is often limited by the poorly defined nature of the contact between the molecules and the metal surface. We describe a method to wire molecules into gaps in single-walled carbon nanotubes (SWNTs). Precise oxidative cutting of a SWNT produces carboxylic acid-terminated electrodes separated by gaps of ≤ 10 nanometers. These point contacts react with molecules derivatized with amines to form molecular bridges held in place by amide linkages. These chemical contacts are robust and allow a wide variety of molecules to be tested electrically. In addition to testing molecular wires, we show how to install functionality in the molecular backbone that allows the conductance of the single-molecule bridges to switch with pH.

One of the greatest challenges in molecular electronics is the ill-defined bonding between molecules and metal electrodes. For even the most well-studied system, thiolated molecules on Au contacts (1–8), there are no methods to control the type of metal-molecule bonding (9), although the contact itself is thought to dominate the transport properties (10). Even if more conductive contact chemistry is used, such as carbenes on transition metals (11) and on metal carbides (12), molecular-scale metal electrodes are extremely difficult to fabricate and lack specific chemistry for molecular attachment at their ends.

An improved strategy would create a well-defined covalent bond between the electrode and the molecule with a limited number of molecular bonding sites and would be intrinsically molecular in scale. Here we describe such a system, in which cut single-walled carbon nanotubes (SWNTs) (13, 14) are covalently attached to molecules through amide linkages. All of the ele-

ments in the resulting molecular circuits are naturally at small dimensions because the SWNTs are one-dimensional (1D) conductors or semiconductors (15–17) that are intrinsically the same size as the molecules being probed. We have tested a number of different types of molecules, including species with chemical functionality that allows the molecular conductance to be switched.

The strategy for attaching molecular wires to SWNT electrodes is to cut them by local oxidation, leaving two ends that are capped with the product of this oxidation and separated by a molecular-scale gap. Given the strongly oxidizing conditions used here, we expect a prevalence of carboxylic acid groups on the cut ends of these SWNTs (18). A molecular bridge with amine end groups is then chemically attached to the carboxylic acid ends by a dehydration reaction to form the amide linkage (18–21). The amine-containing aromatics used here are common, easily prepared, and stable under the reaction conditions. The amine functions avoid one of the serious

drawbacks of thiol chemistry, the oxidative oligomerization of dithiols. The amine-attachment chemistry is well developed in peptide synthesis, and the amide bonds that are formed are extremely stable. Moreover, much of the detrimental stochastic switching (9) and lateral surface mobility of metal grains (22) that plague thiols on gold are absent in these covalently bonded junctions.

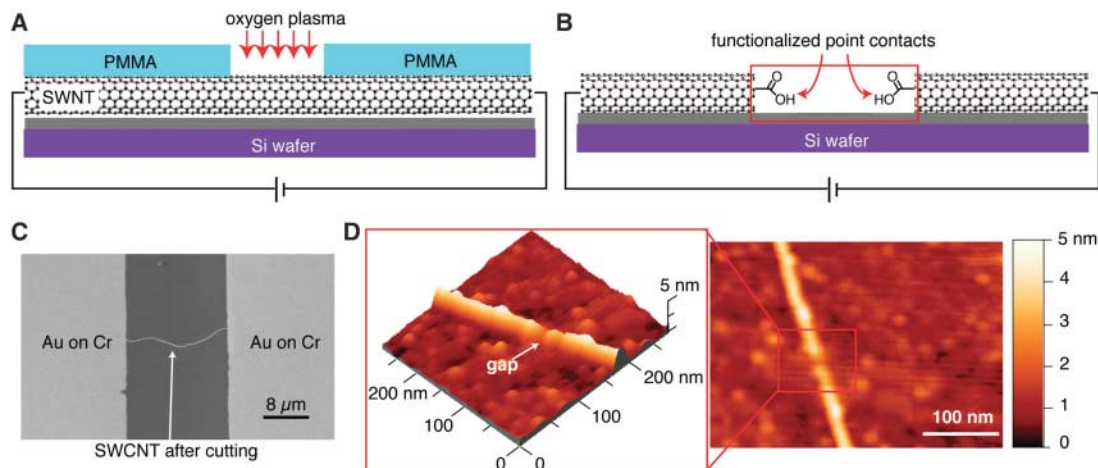
We grew the individual SWNTs by chemical vapor deposition on degenerately doped silicon wafers with 300 nm of thermally grown SiO₂ on their surface (23). The SWNTs grown in this way are ~ 1 to 2 nm in diameter (23). Metallic electrodes (5 nm of Cr overlaid by 50 nm of Au) separated by 20 μm were deposited through a shadow mask onto the SWNTs. The nanotube devices were electrically tested using the metal pads as source (S) and drain (D) contacts and the silicon substrate as a back gate (G).

The method used to create molecular-scale gaps with carboxylic acid end-group functionality is illustrated in Fig. 1, A and B. First, a window that is less than 10 nm in size was opened in a spin-cast layer of polymethylmethacrylate (PMMA) by using ultrahigh-resolution electron-beam lithography (fig. S1) (24). The nanotubes were then locally cut through the open window via oxygen plasma ion etching (250 mTorr, 50 W RF power, 10 s exposure) (24). This gap is too small to be imaged in the scanning electron microscope (Fig. 1C), but it can be located and directly imaged with atomic force microscopy (AFM) (Fig. 1D). The relatively large size of the AFM tip makes it difficult to determine with precision how small these gaps are. For the AFM micrographs in Fig. 1D, we take the imaging

¹Department of Chemistry, ²Department of Physics, ³Department of Mechanical Engineering, ⁴Department of Applied Physics/Applied Mathematics, ⁵The Columbia University Center for Electronics of Molecular Nanostructures, Columbia University, New York, NY 10027, USA.

*To whom correspondence should be addressed. E-mail: cn37@columbia.edu (C.N.), pkim@phys.columbia.edu (P.K.)

Fig. 1. (A) Precise cutting of SWNTs with an oxygen plasma introduced through an opening in a window of PMMA defined with e-beam lithography. **(B)** Oxidative opening of a tube produces two point-contacts functionalized on their ends with carboxylic acids and separated by as little as 2 nm. **(C)** Scanning electron micrograph of a SWNT with Au on Cr leads that had been cut using e-beam lithography and an oxygen plasma. **(D)** AFM image of the gap cut into the SWNT. (Inset) Height profile of the isolated tubes. The diameter of the SWNT is 1.6 nm, estimated from the height profile.



convolution of the AFM tip size into account and set an upper bound on the size of a typical gap opened in the SWNTs of ~ 10 nm for the processing conditions described above.

The statistical variability of the plasma etch process creates ensembles of SWNT devices with gaps of less than 10 nm. We speculate, on the basis of previous oxidation studies of SWNTs (18, 25, 26), that the oxidation creates or nucleates at a defect on the side wall (either present before etching or induced by the plasma) and continues to oxidatively erode the tube. We measure the electrical transport properties of the SWNT before and after oxidative etching to determine the yield of completely cut tubes. Longer

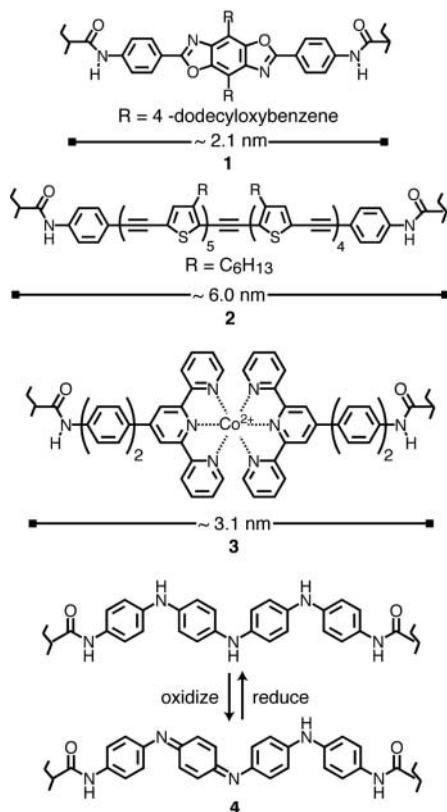
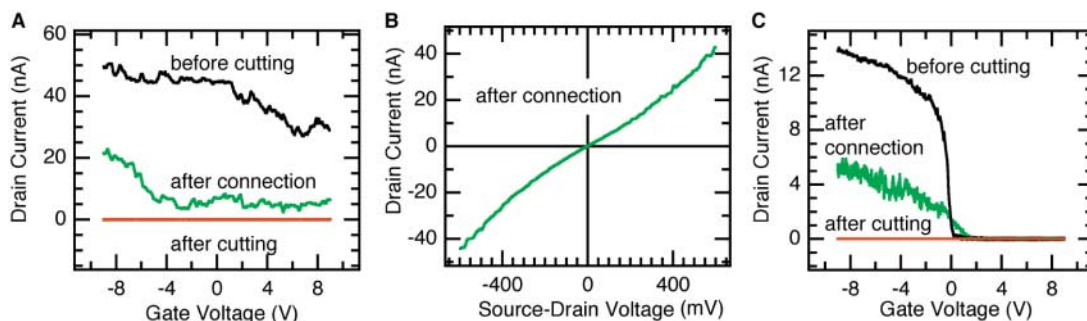


Fig. 2. Molecular bridges (1 to 4) spanning carbon nanotube leads. Oligoaniline 4 provides a redox- and pH-sensitive molecular bridge.

Fig. 3. (A) Metallic SWNT electrodes connected with 1 drain current (I) in the device as a function of the gate voltage (V_g) at $V_{SD} = 50$ mV for a metallic tube reconnected with 1. Electrical measurements were made before cutting (black curve), after cutting with an oxygen plasma (red curve), and after connection (green curve). (B) Drain current (I_D) as a function of source-drain voltage (V_{SD}) with no gate bias. (C) Drain current in the device as a function of the gate voltage (V_g) at $V_{SD} = 50$ mV for a semiconducting SWNT connected with 1. Colors are as described in (A).



etch times give higher yields of the cutting but lower the yields of the chemical connection reactions discussed below. We intentionally shorten the etch time so that the average gap can be narrower than the window in the PMMA. Under optimized conditions, ~ 20 to 25% of the tubes are completely cut among ~ 2500 devices tested.

We synthesized the corresponding molecular wires (1 to 4) that were terminated with the requisite amine functionality according to the procedures outlined in (24). We attached the wires to the cut nanotube ends by immersing the diamines and the SWNT devices into a pyridine solution containing the well-known carbodiimide dehydrating/activating agent EDCI (24, 27). After reaction, the devices were removed from the solution, rinsed with fresh solvent, dried, and then tested electrically. Some of the devices that were previously open showed a finite and measurable conductance after reaction.

The various molecular bridges that we have incorporated into the nanotube electrodes with this technique are shown in Fig. 2. The cruciform π -systems (1) (28) and the longer oligothiophenylene (2) (29) have a path of through conjugation for electrical conduction and lateral side chains that make them highly soluble. These side chains also provide considerable width to these molecules. For example, the width of 1 with its aryl dodecylxy side chains fully extended would be ~ 4.3 nm. This value is substantially greater than the diameter of typical SWNTs used in this experiment (~ 1 to 2 nm). Similarly, the terpyridyl-containing molecules (3) have a substantial width compared to the diameter of a SWNT. Given the volume occupied by 1, 2, and 3, it is difficult to bridge this gap with more than one molecule and certainly not more than two. The oligoaniline (4) is thinner, and we estimate, on the basis of its molecular volume, that a maximum of seven oligoanilines could bridge an orthogonally cut SWNT gap. The number of reactive sites is reduced further if we assume that the gaps are unevenly cut.

These amidation reactions allowed us to calibrate the etch process itself because the different species can be used as molecular rulers. For example, under optimized conditions, the yield for connection of 1 for more than 200

reactions is $\sim 10\%$. Using longer etch times, which give the larger gaps, reduces the yield of the coupling reaction with 1. Moreover, molecules of length similar to that of 1 give similar yields in these reactions, implying that the yield is dominated by the statistics of having two functional groups appropriately spaced for bridging. Under identical conditions, the longer molecules (2 and 3) gave lower yields in their connection reactions ($\sim 5\%$). To determine whether the greater length of the molecule was limiting the yield of successful contacts, we prepared a mixture of three oligomers based on 2 that ranged in length from 2 to 6 nm. The yield increased to $\sim 20\%$ for the connection reaction with this mixture.

Electrical measurements on devices before cutting, when cut, and after connection with 1 are shown in Fig. 3. The black curves show the source-drain current (I) plotted against the gate voltage (V_g) at constant S-D bias voltage ($V_{SD} = 50$ mV) for two devices before cutting. The device in Fig. 3, A and B, before cutting shows metallic behavior, and the one in Fig. 3C shows typical p-type semiconducting behavior. The red traces, taken after cutting, show no conductance down to the noise limit of the measurement (≤ 2.0 pA). The green traces show the devices after molecular connection of the SWNT leads. Similar I - V_{DS} curves (figs. S2 and S3) are shown for connection with the other molecular bridges (2 to 4) (24). In all cases, the reconnected devices recovered their original metallic or semiconducting behavior at reduced values of I , indicating that the gate modulates the nanotube conductance more strongly than that of the molecules.

The resistance, and thus the molecular conductance, can be estimated from the drop in current after molecular connection. For example, the resistance of the metallic tube connected in Fig. 3, A and B, with the cruciform molecule (1) increases from ~ 1 megohm before cutting to ~ 5 megohm after connection with the $V_{SD} = 50$ mV in the linear response regime. The molecular conductance for 1 in this device is calculated to be $6.4 \times 10^{-3} e^2/h$. Table 1 displays similar data for 2 to 4 in SWNT gaps. In some cases, the conductance is greater than $10^{-2} e^2/h$. Moreover, the I - V curves at low temperature (down to 1.6 K; figs. S4 and S5) have a wealth of structure

Table 1. SWNT device properties before cutting and after molecular connection.

Tube type	Before cutting		After molecular connection	
	R^* (megohm)	Molecule	R^* (megohm)	Molecular conductance (e^2/h)
Metallic	1.0	1	5.0	6.4×10^{-3}
Semiconducting	3.6	1	10.0	4.0×10^{-3}
Semiconducting	1.1	2	5.0	6.6×10^{-3}
Metallic	0.2	3	0.6	6.4×10^{-2}
Semiconducting	0.6	3	125	2.0×10^{-4}
Semiconducting	1.3	4	50.0	5.2×10^{-4}

* R is the total resistance for the device. For the semiconducting tubes this refers to ON-state resistance with $V_{SD} = 50$ mV.

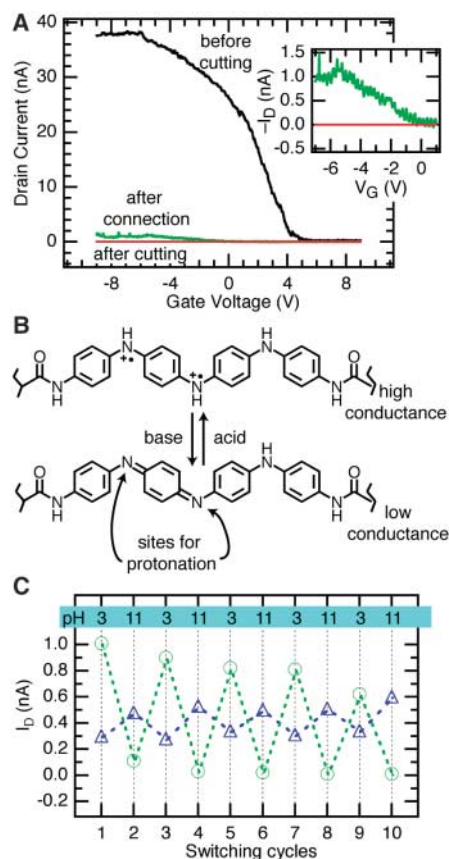


Fig. 4. Oligoaniline **4** connected to SWNT electrodes. **(A)** Drain current (I_p) in the device as a function of the gate voltage (V_g) at $V_{SD} = 50$ mV for a semiconducting tube connected with **4**. Electrical measurements were made before cutting (black curve), after cutting with oxygen plasma (red curve), and after connection (green curve). Inset is a magnified y scale showing the I - V curves after cutting and connection. **(B)** Protonation and deprotonation to give high- and low-conductance forms of oligoaniline **4**. **(C)** Green circles show the ON-state resistance for **4** when alternately immersed in solutions of low and high pH. The blue triangles show small changes in ON-state resistance for **2** when alternately immersed in solutions of low and high pH.

and features that gradually broaden and eventually disappear with increasing temperature (30). Being able to match the electronic levels of the molecule to a nanotube of a specific diameter and

chirality, in principle, offers the opportunity to optimize the conductance. One factor that hampers our ability to extract more quantitative information is that these values vary for any given molecule. Variations in the conformation of the molecules on the substrate within the SWNT gap, the possibility of a second molecular bridge, and the lack of atomic-level precision in the cutting procedure are challenges for future studies to overcome.

Control experiments were performed to rule out artifacts from the connection reaction. Gaps placed in a pyridine solution of the coupling agent without the conjugated diamines did not show any connected devices. Furthermore, when we immersed these same gaps in a solution that contains the cruciform diamine (**1**) along with an aliquot of fresh coupling reagent, some of the devices then became connected. In another experiment, we used 1,12-diaminododecane because it is about the same length as the cruciform molecule but lacks the conjugated backbone. Again, all of the devices showed no detectable current and remained so when a conjugated diamine was added, presumably because the carboxylic acid sites were blocked by the alkyl amine. To determine if molecular aggregates were responsible for the conduction, we tested a monoamine of the cruciform or a cruciform that completely lacked the amine groups, and only open circuits resulted. All of these control experiments were performed on ~ 50 devices in order to yield a statistically significant null result.

The covalent linkages are quite robust and tolerate broad changes in environment, and we explored how these devices responded to external stimuli such as changes in temperature and pH. The response to changes in pH for the oligoaniline diamine **4** is shown in Fig. 4. The electrical characteristics for this device before cutting, after cutting, and after joining with the oligoaniline diamine are similar to those detailed for **1** to **3**. We expected that the oligoaniline would be oxidized to the emeraldine form (shown in Fig. 2) during the reaction and become pH sensitive, because the protonated form is more conductive (Fig. 4B) (31). We performed a series of protonations (pH = 3) and deprotonations (pH = 11) while monitoring the current changes at saturation for devices that were rinsed, dried, and tested. The molecular conductance changed by nearly an order of magnitude, from $\sim 5.2 \times 10^{-4} e^2/h$ at low pH to $\sim 5.0 \times 10^{-5} e^2/h$ at high pH over many

switching cycles (Fig. 4C). These devices provide a local probe for monitoring pH on the basis of one or only a few molecules.

We also performed the same experiment on devices connected with **2**, which lacks basic nitrogens and thus should not switch with pH. The blue trace in Fig. 4C shows that the conductance of **2** changed only slightly with pH, and the change was in the opposite direction to that for the device connected with the pH- and redox-active oligoaniline **4**. Another possible cause of the pH switching in the oligoaniline devices could be charge transfer from a polyaniline that was attached but not necessarily spanning the SWNT gap (32). Amines (**16**), particularly polyanilines (32), can associate with the SWNT surface and might cause pH sensitivity that is unrelated to molecular conduction. We therefore immersed an uncut device in a solution of the polyaniline diamine (**4**) (24). The relative change upon protonation/deprotonation was small for these devices and in the opposite direction to that for the device connected with oligoaniline (fig. S6).

In conclusion, we present experiments that overcome the difficulty of creating covalent contact to individual molecules and reveal a way to harness the diversity and functionality inherent to molecules in electrical devices. In addition to their potential use as molecules in circuits, sensors, and switches, these devices promise a deeper understanding of electron transfer at the molecular scale.

References and Notes

- M. A. Reed, C. Zhou, C. J. Muller, T. P. Burgin, J. M. Tour, *Science* **278**, 252 (1997).
- A. Salomon *et al.*, *Adv. Mater.* **15**, 1881 (2003).
- J. Chen, M. A. Reed, A. M. Rawlett, J. M. Tour, *Science* **286**, 1550 (1999).
- X. D. Cui *et al.*, *Science* **294**, 571 (2001).
- M. Mayor *et al.*, *Angew. Chem. Int. Ed.* **42**, 5834 (2003).
- M. Mayor, H. B. Weber, *Angew. Chem. Int. Ed.* **43**, 2882 (2004).
- J. Park *et al.*, *Nature* **417**, 722 (2002).
- N. B. Zhitenev, A. Erbe, Z. Bao, *Phys. Rev. Lett.* **92**, 186805 (2004).
- G. K. Ramachandran *et al.*, *Science* **300**, 1413 (2003).
- H. Basch, R. Cohen, M. A. Ratner, *Nano Lett.* **5**, 1668 (2005).
- G. S. Tulevski, M. B. Myers, M. S. Hybertsen, M. L. Steigerwald, C. Nuckolls, *Science* **309**, 591 (2005).
- M. Siaz, P. H. McBreen, *Science* **309**, 588 (2005).
- P. Qi *et al.*, *J. Am. Chem. Soc.* **126**, 11774 (2004).
- K. Tsukagoshi, I. Yagi, Y. Aoyagi, *Appl. Phys. Lett.* **85**, 1021 (2004).
- J. Appenzeller, J. Knoch, M. Radosavljevic, P. Avouris, *Phys. Rev. Lett.* **92**, 226802 (2004).
- H. Dai, *Acc. Chem. Res.* **35**, 1035 (2002).
- S. J. Tans, A. R. M. Verschueren, C. Dekker, *Nature* **393**, 49 (1998).
- S. Niyogi *et al.*, *Acc. Chem. Res.* **35**, 1105 (2002).
- P. W. Chiu, M. Kaempgen, S. Roth, *Phys. Rev. Lett.* **92**, 246802 (2004).
- U. Dettlaff-Weglikowska *et al.*, *Curr. Appl. Phys.* **2**, 497 (2002).
- E. Artukovic, M. Kaempgen, D. S. Hecht, S. Roth, G. Gruner, *Nano Lett.* **5**, 757 (2005).
- A. A. Houck, J. Labaziewicz, E. K. Chan, J. A. Folk, I. L. Chuang, *Nano Lett.* **5**, 1685 (2005).
- L. Huang, X. Cui, B. White, S. P. O'Brien, *J. Phys. Chem. B* **108**, 16451 (2004).
- Experimental details on SWNT device fabrication, electron beam lithography, and oxidative cutting can be found in

- the Supporting Online Material, along with low-temperature current-voltage curves and experimental details for the synthesis and reactions of **2** to **4**.
25. K. J. Ziegler *et al.*, *Nanotechnology* **16**, 5539 (2005).
 26. Z. Gu, H. Peng, R. H. Hauge, R. E. Smalley, J. L. Margrave, *Nano Lett.* **2**, 1009 (2002).
 27. A. Williams, I. T. Ibrahim, *Chem. Rev.* **81**, 589 (1981).
 28. J. E. Klare, G. S. Tulevski, C. Nuckolls, *Langmuir* **20**, 10068 (2004).
 29. Details for the preparation of **2** to **4** can be found in the Supporting Online Material.
 30. It is also noted that at low temperature the differential conductance, dI/dV_{DS} , develops a series of peaks as V_{DS} changes. The position of these peaks shifts as a function of the applied gate voltage. As an example, the low-temperature $I-V_{DS}$ and dI/dV_{DS} curves for **1** are shown in the Supporting Online Material.
 31. A. G. MacDiarmid, *Angew. Chem. Int. Ed.* **40**, 2581 (2001).
 32. C. Klinke, J. Chen, A. Afzali, P. Avouris, *Nano Lett.* **5**, 555 (2005).
 33. We are grateful to H. Stormer for enlightening discussions. We acknowledge primary financial support from the Academic Quality Fund (Columbia University), the Nanoscale Science and Engineering Initiative under NSF Award Number CHE-0117752, and the New York State Office of Science, Technology, and Academic Research (NYSTAR). C.N. thanks the American Chemical Society Petroleum Research Fund Type G (grant 39263-G7), the Camille Dreyfus Teacher Scholar Program (2004), and the Alfred P. Sloan Fellowship Program

(2004). P.K. thanks the NSF CAREER (DMR-0349232) and Defense Advanced Research Projects Agency (N00014-04-1-0591). J.E.K. thanks the American Chemical Society Division of Organic Chemistry sponsored by Organic Syntheses for a fellowship. I.W.T. thanks the NSF for a predoctoral fellowship.

Supporting Online Material

www.sciencemag.org/cgi/content/full/311/5759/356/DC1
Materials and Methods
Figs. S1 to S6
References and Notes

5 October 2005; accepted 15 December 2005
10.1126/science.1120986

Real-Space Observation of Helical Spin Order

Masaya Uchida,^{1*} Yoshinori Onose,^{1†} Yoshio Matsui,² Yoshinori Tokura^{1,3,4}

Helical spin order in magnetic materials has been investigated only in reciprocal space. We visualized the helical spin order and dynamics in a metal silicide in real space by means of Lorentz electron microscopy. The real space of the helical spin order proves to be much richer than that expected from the averaged structure; it exhibits a variety of magnetic defects similar to atomic dislocations in the crystal lattice. The application of magnetic fields allows us to directly observe the deformation processes of the helical spin order accompanied by nucleation, movement, and annihilation of the magnetic defects.

Magnetic materials are generally characterized by spin moments on respective atomic sites aligned all parallel or site-alternately antiparallel. However, many exceptions to this rule exist in which the direction of spin moments varies in space. A prototypical example is the gradual moment variation (Bloch type or Néel type) within the magnetic domain wall region in a ferromagnet (1) or the somewhat long-period (over several atomic sites) spin density wave as observed in Cr metal (2). The helical spin order (Fig. 1A) is another such example: Spins on some crystallographic planes are all parallel, but their direction rotates by a constant angle in going from one plane to a neighboring plane along the helical axis. The helical spin order was first proposed as a way to interpret neutron diffraction results for MnO₂ crystal (3). Similar helical spin orders have been observed in materials such as rare-earth metals and alloys (4) as well as members of the metal silicide family, including MnSi (5, 6) and Fe_{1-x}Co_xSi (0.05 ≤ x ≤ 0.8) (7, 8).

The relative orientation of spin moments between magnetic planes affects the flow of electric current. The control of the spin-dependent charge transport in terms of the manipulation of the local magnetic structure forms the basis of spin-electronics or spintronics (9–12), as exemplified by the magnetoresistive field sensor in computer hard disks and the magnetic tunneling junction in magnetic random access memory (MRAM). In this context, the helical spin order can be viewed as a regular array of the magnetic domain walls every helical period. Therefore, the real-space observation of the local modification or deformation of the helical order (as induced by temperature change, magnetic field, and current injection) would provide a challenging arena to study the nanometric magnetic domain structure as well as to explore the possible spintronic application of such a self-organized magnetic nanostructure.

The family of Fe_{1-x}Co_xSi with cubic but non-centrosymmetric (B20) structure is known to

exhibit a helical spin order, with a relatively long period (>30 nm) in a concentration range 0.05 ≤ x ≤ 0.8 (7, 8, 11). The helical spin order is due to the Dzyaloshinsky-Moriya (DM) interaction because of the lack of centrosymmetry of the lattice (13–16). The helix period is governed by the ratio of the DM interaction to the ferromagnetic spin exchange interaction (15, 16). The Néel temperature T_N and the helix period for the x = 0.5 crystal we investigated here are 38 K and 90 nm along the [100] direction, respectively.

Figure 2 shows a typical image of the helical spin order of Fe_{0.5}Co_{0.5}Si as obtained by Lorentz transmission electron microscopy (17). Shown in Fig. 2, A and B, are overfocused Lorentz images taken near the [001] zone axis orientation at 40 and 20 K, respectively. The image at 20 K (< T_N) clearly shows periodic stripe patterns running normal to the [100] axis. In the focused image the patterns disappeared, confirming that the image is magnetic in origin. The magnetization distribution obtained by the transport of intensity equation (TIE) analysis (18, 19) of the over- and under-focused images is shown in Fig. 2C. The direction and amplitude of the magnetization are represented by changes in color and brightness, respectively. The green and violet stripe pairs in the figure reflect the regions with opposite magnetic orientation; the darker area indicates the smaller amplitude of the local magnetization. The sinusoidal modulation in Fig. 2D (a profile of the amplitude of the magnetization along the line indicated in Fig. 2C) indicates that the spin order is helical, with a period of 90 nm along [100], in good agreement with the results determined by neutron diffraction (7, 8).

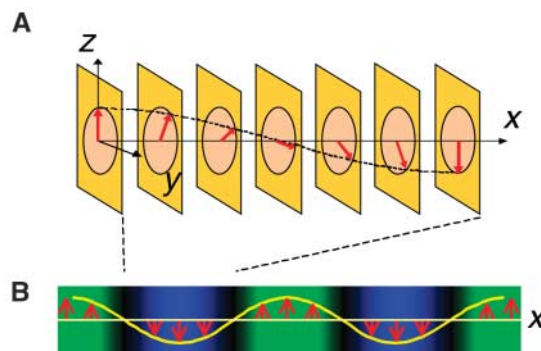


Fig. 1. Illustration of helical spin order. (A) Helical spin order with the helical axis along the x axis in an orthogonal xyz system. Spins are all parallel at a yz plane, and their direction rotates by a constant angle from one plane to a neighboring plane along the helical axis. (B) Magnetization distribution projected on the xy plane for this helical spin order, which changes as a sinusoidal wave.

¹Spin SuperStructure Project, Exploratory Research for Advanced Technology (ERATO), Japan Science and Technology Agency (JST), Tsukuba 305-8562, Japan. ²Advanced Materials Laboratory, National Institute for Materials Science (NIMS), Tsukuba 305-0044, Japan. ³Correlated Electron Research Center (CERC), National Institute of Advanced Industrial Science and Technology (AIST), Tsukuba 305-8562, Japan. ⁴Department of Applied Physics, University of Tokyo, Tokyo 113-8656, Japan.

*To whom correspondence should be addressed. E-mail: uchida.masaya@aist.go.jp

†Present address: Department of Physics, Princeton University, Princeton, NJ 08543, USA.